Stability analysis of the flow in a cubical cavity heated from below

D. Puigjaner[1], C. Simó[2], F.X. Grau[3] and Francesc Giralt[4,*]

(1) Dept. Enginyeria Informàtica i Matemàtiques, ETSE, Univ. Rovira i Virgili , Tarragona, Catalunya, Spain.

(2) Dept. Matemàtica Aplicada i Anàlisi, Fac. Matemàtiques, Univ. de Barcelona, Barcelona, Catalunya, Spain.

(3) Dept. Enginyeria Mecànica, ETSEQ, Univ. Rovira i Virgili, Tarragona, Catalunya, Spain.

(4) Dept. Enginyeria Química, ETSEQ, Univ. Rovira i Virgili, Tarragona, Catalunya, Spain.

(*) Corresponding author. Phone:34977559638; Fax:34977559621; e-mail:fgiralt@etseq.urv.es

Abstract

A numerical study of bifurcations and stability of stationary convective flows in cubical and rectangular enclosures heated from below was carried out using a Galerkin spectral method with a complete, divergent-free set of trial functions satisfying all boundary conditions. A path-continuation method was applied to determine the stationary solution of the non–linear governing equations as a function of Rayleigh number within the range $Ra_c \leq Ra \leq 7 \times 10^4$. The eigenvalue problem associated with stability analysis of the non-linear stationary solutions along the bifurcated branches was solved using the QR algorithm. Four different bifurcations from the conductive state were identified for $Ra < 10^4$. At the first transition ($Ra_c \leq 3389$) a x–roll and a diagonal–roll were formed. While the former is stable, the latter is slightly unstable with instability increasing with Ra. The second bifurcation yielded an unstable four–roll structure that stabilized at $Ra \simeq 8900$. The third and fourth bifurcations resulted in highly unstable structures. The effect of changing aspect ratios on the bifurcation Ra for rectangular cavities was also studied. There is reasonable agreement between the critical Rayleigh numbers, the type of structures developed, and the velocity and temperature fields predicted by the current stability analysis and previous numerical and experimental results reported in the literature. The convergence of the method is consistent with the number of modes used and the results clarify inconsistences of previous DNS and experimental results published in the literature.

1 Introduction

Convection in rectangular cavities and within horizontal annuli has been widely studied because of its fundamental interest in relation to the genesis and evolution of flow patterns and the onset of unsteadiness. These flow systems also have many technological applications. Lid–driven and natural convection flows in such geometries have been thoroughly investigated for several different boundary conditions[1,2] since they are also frequently employed as benchmark problems for two and three dimensional Navier–Stokes solvers[3–5]. For example, a complete solution using the spectral Galerkin method of a recently formulated benchmark problem[5] devoted to the parametric study of Rayleigh–Bénard flow in rectangular enclosures has been described by Gelfgat[4]. A new three-dimensional (3D) mode of centrifugal–flow instability in lid–driven cavities with comparable length and width has been recently identified[6] by means of a second–order finite volume discretization of the governing equations on a staggered grid. In addition, the stability of buoyancy–induced flows between concentric cylinders has been investigated by Dyko et.al.[7] by using both linear theory and the energy method. These authors also report a thorough numerical and experimental study of the development of secondary flow in the form of a spiral vortex for an annulus of moderate gap size. Finally, it could be mentioned the combined application of the LES and RANS modelling[8] to study transient Rayleigh-Bénard flow at high Rayleigh numbers.

The clearest way from the fundamental point of view to carry out a stability analysis of convection flows inside enclosures is to consider a fluid layer of infinite horizontal extent[9–13]. Nevertheless, two-dimensional (2D) flows in plane rectangular enclosures cannot be rigorously realized in practice as sidewalls play an important role in finite flow configurations[14], i.e., the end wall bias or "contaminations" is unavoidable. Alternatives are to carry out experiments in toroidal cavities of rectangular (or circular) cross-sections[15] since they are devoid of end wall effects or to consider the corresponding 3D cases. Several methods have been used in the past to study bifurcations and stability in convective 3D flows. One choice is time-forward integration of the non-stationary equations[16,17,22]. However, time–dependent methods involve intensive CPU-time consuming calculations, are affected by initial conditions, and are unable to follow the evolution of unstable solutions that could lead to stable ones at secondary bifurcations. Unlike direct numerical simulation approaches, stability analysis methods calculate more effectively critical points. The variation of these critical points with relevant parameters can be determined in a straightforward way by applying a path continuation method[4,5,9,18,21,23,26]. It should be noted that the multiplicity of numerical solutions leads to an eigenvalue problem whose order is equal to the number of unknown scalar variables used by the numerical method to approximate the solution (number of finite elements, grid size in finite differences, etc.). The order of the eigenvalue problem may be reduced if the Galerkin method with a divergent–free basis satisfying all the boundary conditions is applied[4,9,19].

The first bifurcation for the transition from the conductive state to the onset of convection is well documented in the literature for 2D rectangular cavities and for 3D enclosures with a variety of width/height and length/height aspect ratios (h_1, h_2)[9–14]. The aim of the current work is to study the bifurcations and stability of the stationary convective flow in a cubical cavity heated from below by using a Galerkin spectral method. A path continuation method is applied to explain why a recent experimental PIV study[20] reports a four–roll structure for the Rayleigh-Bénard flow in a cubical cavity at moderate Rayleigh numbers, in contrast to the solely single roll structure reported by Catton[21] or to the multiplicity of apparently stable flow structures educed by time–forward numerical computations[16,22]. This contradiction has been solved first by completing the divergent-free basis functions proposed by Catton[21], and second by determining the bifurcation diagram of a natural flow that by its inherent lack of preferred direction generates vertical modes different from those in rectangular enclosures. The bifurcation diagram displays the stability and domains of existence of the alternative steady solutions that arise at singular points as a function of the Rayleigh number. Both, stable and unstable branches are followed using a path-continuation algorithm applied to the non–linear stationary governing equations. At any point along the different bifurcating branches the stability of the flow is studied by linearizing the equations around that point. Thus, the method extends the analysis beyond the regions around singular points. Unstable flow structures are also considered because they can become stable beyond their critical Rayleigh number. In addition to the cubical cavity problem, the effect of varying the aspect ratios h_1, h_2 on the onset of convection is also reported. In the next section the physical model and the non-linear governing equations are presented. The linear analysis of the problem and results are included and discussed in section 3 while the nonlinear analysis and bifurcation diagram are discussed in section 4.

2 Physical model and governing equations

The physical model and the coordinate system are shown in Figure 1. The two horizontal plates are isothermal and the four vertical walls are considered perfectly insulated. The domain covered by a parallelepipedic cavity, scaled by the characteristic height L, is given by $\Omega = [-\frac{h_1}{2}, \frac{h_1}{2}] \times [-\frac{h_2}{2}, \frac{h_2}{2}] \times [-\frac{1}{2}, \frac{1}{2}]$.

In the following analysis ρ is the density of the fluid, g is the acceleration of gravity, θ_c and θ_h are the temperature at the top and the bottom of the cubical region, respectively, $\Delta\theta = \theta_h - \theta_c$, and β, ν and α are respectively the coefficients of thermal expansion, kinematic viscosity and thermal diffusivity. All these physical properties are assumed to be constant. The Boussinesq approximation is used to determine the effect of density (ρ) in the buoyancy term.

The dimensionless coordinates are denoted as x, y and z. The characteristic scales for velocity $\vec{V} = (v^{(1)}, v^{(2)}, v^{(3)})$, temperature ($\theta$), time ($t$) and pressure ($p$) are $q_0 = [\beta(\Delta\theta)gL\alpha/\nu]^{\frac{1}{2}}$, $\Delta\theta$, L^2/α and $\rho\nu q_0/L$, respectively[23]. The application of the Galerkin method to the governing linearized equations yields a linear self–adjoint operator when these scales are used. This self-adjointness guarantees that the onset of convection occurs via a stationary state[24] (the principle of exchange of stabilities).

The steady conductive state is described by a linear profile $\theta_s(z) = \theta_c + (z + 1/2)\Delta\theta$ and by $\vec{V}_s = 0$. Let $\theta(x, y, z, t)$ be the difference between the temperature within the domain Ω and θ_s. The governing Boussinesq nonlinear equations are

$$div\,\vec{V} = 0, \tag{1}$$

$$\frac{1}{Pr}\frac{\partial \vec{V}}{\partial t} - \nabla^2 \vec{V} + \frac{Ra^{\frac{1}{2}}}{Pr}\sum_{i=1}^{3} v^{(i)} D_i \vec{V} - Ra^{\frac{1}{2}}\theta\,\vec{K} + \vec{\nabla}\,p = 0, \tag{2}$$

$$\frac{\partial \theta}{\partial t} - \nabla^2 \theta + Ra^{\frac{1}{2}}\sum_{i=1}^{3} v^{(i)} D_i \theta - Ra^{\frac{1}{2}} v^{(3)} = 0 \tag{3}$$

with boundary conditions

$$\vec{V} = \theta = 0 \text{ on } |z| = \frac{1}{2}, \quad \vec{V} = \frac{\partial \theta}{\partial x} = 0 \text{ on } |x| = \frac{h_1}{2}, \quad \vec{V} = \frac{\partial \theta}{\partial y} = 0 \text{ on } |y| = \frac{h_2}{2}. \tag{4}$$

In equations (2) and (3) the Rayleigh number and the Prandtl number are defined as $Ra = \beta(\Delta\theta)gL^3/\alpha\nu$ and $Pr = \nu/\alpha$, respectively, and $\vec{K}$ denotes the vector $(0,0,1)$.

3 Linear stability problem

3.1 Equations

The linearization of the steady state part of equations (1–3) yields,

$$div\,\vec{V} = 0, \tag{5}$$

$$\nabla^2 \vec{V} + Ra^{\frac{1}{2}}\theta\,\vec{K} - \vec{\nabla}\,p = 0, \tag{6}$$

$$\nabla^2 \theta + Ra^{\frac{1}{2}}\, v^{(3)} = 0 \tag{7}$$

with the same boundary conditions (4). From this set of linear equations it is clear that the onset of convection is independent of the Prandtl number.

The systems (1–3) and (5–7), with boundary conditions (4), are not separable but approximate solutions may be obtained using the Galerkin procedure.

3.2 Numerical procedure

Let us consider

$$T = \{\phi \in L^2(\Omega) \,|\, \phi_n = 0 \text{ on } |z| = \frac{1}{2}, \ \frac{\partial \phi_n}{\partial x} = 0 \text{ on } |x| = \frac{1}{2}, \ \frac{\partial \phi_n}{\partial y} = 0 \text{ on } |y| = \frac{1}{2}\} \tag{8}$$

and

$$E = \{\vec{\psi} \mid D_i \psi^{(k)} \in L^1(\Omega),\ div\, \vec{\psi}_n = 0,\ \vec{\psi}_n = 0 \text{ on } \partial\Omega\}\,. \tag{9}$$

Solutions of equations (5–7) are approximated as a truncated series

$$\begin{pmatrix} \vec{V} \\ \\ \theta \end{pmatrix} = \sum_{k=1}^{N} c_k \begin{pmatrix} \vec{\psi}_k \\ \\ 0 \end{pmatrix} + \sum_{k=1}^{M} d_k \begin{pmatrix} \vec{0} \\ \\ \phi_k \end{pmatrix}, \tag{10}$$

where $\{\vec{\psi}_k\}$ and $\{\phi_k\}$ form complete sets of functions on the spaces T and E respectively. In other words, the unknown solutions (10) are localized in the subspace of divergent–free functions satisfying all the boundary conditions. Pressure p is not explicitly expanded because it does not appear in the final equations.

Following the well-known Galerkin method[25] the truncated series (10) is introduced in the field equations (5–7), which are then multiplied by the trial functions and integrated over the fluid domain Ω. Thus, the set of partial differential equations (5–7) is replaced by the set of algebraic equations

$$M(Ra) \begin{pmatrix} c \\ \\ d \end{pmatrix} = \vec{0}, \tag{11}$$

where

$$M(Ra) = \begin{pmatrix} A & Ra^{\frac{1}{2}} B^T \\ \\ Ra^{\frac{1}{2}} B & C \end{pmatrix} \tag{12}$$

and

$$(c, d)^T = (c_1, \cdots, c_N, d_1, \cdots, d_M)^T\,. \tag{13}$$

In equation (12) A, B and C are $N \times N$, $M \times N$ and $M \times M$ matrices, respectively, defined as,

$$A(i,j) = \nabla^2 \vec{\phi}_i \bullet \vec{\phi}_j, \quad B(i,j) = \psi_i \bullet \phi_j^{(3)}, \quad \text{and} \quad C(i,j) = \nabla^2 \psi_i \bullet \psi_j, \tag{14}$$

where $\bullet$ denotes the scalar product.

Continuity equation (5) and boundary conditions (4) are directly satisfied because of the choice of trial functions. The pressure gradient has been eliminated from equation (6) by the Galerkin method since any divergent–free function $\vec{\psi}$ with a vanishing normal component to the boundary is orthogonal to the gradient of any scalar function defined in the same domain.

Non-trivial solutions of equation (11) for $Ra > 0$ can be found as non-trivial solutions $(c, d)^T$ in

$$\left(A^{-1} B^T C^{-1} B - \frac{1}{Ra} I \right) c = 0\,, \tag{15}$$

$$d = -Ra^{\frac{1}{2}} C^{-1} B c\,. \tag{16}$$

Therefore, the problem reduces to an $N \times N$ eigenvalue problem for the Rayleigh number. The critical Rayleigh number Ra_c, i.e., the smallest positive value of Ra for which $\det M(Ra) = 0$, is then the inverse of the greatest positive eigenvalue of $(A^{-1}B^T C^{-1} B)$. This critical value has been estimated using the power method.

The precise form of the trial functions and the proof of its completeness are given in the next section. Note that the trial functions may be separated into eight classes and that those from a different class are orthogonal. The matrix $M(Ra)$ is block diagonal with eight different blocks (M_l, $l = 1, \cdots, 8$), with each block corresponding to one of the eight classes of trial functions mentioned above. Thus, the critical Rayleigh number (Ra_c) is the minimum of the eight values associated to these blocks.

3.3 Trial functions

The objective of the present section is to prove that complete sets of trial functions on the spaces T and E defined in (8, 9) can be built. The method used here to select trial functions is that of Catton[20], but several additional functions have been added to the original Catton's set to ensure its completeness.

It is well known that if the sets $\{f_i\}$, $\{g_j\}$ and $\{h_i\}$ constitute orthogonal bases on $L^2(I_1)$, $L^2(I_2)$ and $L^2(I_3)$, respectively, then the set $\{F_{ijk}(x,y,z) = f_i(x)g_i(y)h_i(z)\}$ is also an orthogonal basis on $L^2(\Omega)$, being $\Omega = I_1 \times I_2 \times I_3$ with I_1, I_2, I_3 closed intervals in $I\!R$. This is important to construct a complete set of trial functions.

Since the eigenfunctions of a Sturm-Liouville problem on an interval I form an orthogonal complete basis for $L^2(I)$ whose elements satisfy boundary conditions[25], the following Sturm-Liouville problems on $I = [-\frac{1}{2}, \frac{1}{2}]$ are considered

$$f'' = af,\ f(-1/2) = f(1/2) = 0; \qquad f'' = af,\ f'(-1/2) = f'(1/2) = 0;$$

$$f^{(IV)} = af,\ f(-1/2) = f(1/2) = 0,\ f'(-1/2) = f'(1/2) = 0\,,$$

whose respective eigenfunctions are

$$\begin{aligned}
&g_k(x):\ \cos((2k-1)\pi x) \quad \text{or} \quad \sin(2k\pi x),\\
&h_k(x):\ \cos(2(k-1)\pi x) \quad \text{or} \quad \sin((2k-1)\pi x),\\
&f_k(x):\ C_k(x) = \frac{\cosh(\lambda_k x)}{\cosh(\lambda_k/2)} - \frac{\cos(\lambda_k x)}{\cos(\lambda_k/2)} \quad \text{or} \quad S_k(x) = \frac{\sinh(\mu_k x)}{\sinh(\mu_k/2)} - \frac{\sin(\mu_k x)}{\sin(\mu_k/2)}\,.
\end{aligned} \tag{17}$$

In expression (17) k is any positive integer and the parameters λ_k and μ_k are the positive roots of equations $\tanh(\lambda_k/2) + \tan(\lambda_k/2) = 0$ and $\tanh(\mu_k/2) - \tan(\mu_k/2) = 0$, respectively.

Since $\Omega = I \times I \times I$, the set

$$\{\phi_{ijk}(x,y,z) = h_i(x)h_j(y)g_k(z)\}_{ijk} \tag{18}$$

with g and h defined by expressions (17), forms an orthogonal complete basis on T.

In order to construct a basis for E this space is splitted according to

$$\begin{aligned} &E = E_1 \oplus E_2, \\ &E_1 = \{v^x = (v^{(1)}, 0, v_1^{(3)})^T \in E \mid \frac{\partial v^{(1)}}{\partial x} = -\frac{\partial v_1^{(3)}}{\partial z}\}, \\ &E_2 = \{v^y = (0, v^{(2)}, v_2^{(3)})^T \in E \mid \frac{\partial v^{(2)}}{\partial y} = -\frac{\partial v_2^{(3)}}{\partial z}\}, \end{aligned} \tag{19}$$

so that any general solution can be obtained as a sum of two kinds of finite rolls. The upper indices x and y define the x–rolls (zero y component of velocity) and the y–rolls (zero x component of velocity) of Catton[21] which are parallel to the y and x axes, respectively. In the present work the solution is expressed as a sum of such rolls in contrast to considering the x–rolls and y–rolls separately, as done by Davis[23].

As a consequence of the equivalences

$$\begin{aligned} &v^x \in E_1 \Longleftrightarrow \exists\, \varphi(x,y,z) \in L^2(\Omega) \text{ verifying } v^{(1)} = -\frac{\partial \varphi}{\partial z} \text{ and } v_1^{(3)} = \frac{\partial \varphi}{\partial x}, \\ &v^y \in E_2 \Longleftrightarrow \exists\, \tau(x,y,z) \in L^2(\Omega) \text{ verifying } v^{(2)} = -\frac{\partial \tau}{\partial z} \text{ and } v_2^{(3)} = \frac{\partial \tau}{\partial y} \end{aligned} \tag{20}$$

it is sufficient to provide suitable bases to expand φ and τ. Therefore the set

$$\left\{\begin{pmatrix} f_i(\frac{x}{h_1})g_j(\frac{y}{h_2})f_k'(z) \\ 0 \\ -\frac{1}{h_1}f_i'(\frac{x}{h_1})g_j(\frac{y}{h_2})f_k(z) \\ 0 \end{pmatrix}\right\}_{ijk} \cup \left\{\begin{pmatrix} 0 \\ g_i(\frac{x}{h_1})f_j(\frac{y}{h_2})f_k'(z) \\ -\frac{1}{h_2}g_i(\frac{x}{h_1})f_j'(\frac{y}{h_2})f_k(z) \\ 0 \end{pmatrix}\right\}_{ijk} \cup \left\{\begin{pmatrix} 0 \\ 0 \\ 0 \\ h_i(\frac{x}{h_1})h_j(\frac{y}{h_2})g_k(z) \end{pmatrix}\right\}_{ijk}, \tag{21}$$

with g, h and f defined by (17), forms a complete basis on E and T. In equation (21) the prime denotes differentiation with respect to the current argument.

Since the boundary conditions are symmetric with respect to the planes $x = 0$, $y = 0$ and $z = 0$, functions g, h and f defined in (17) are either even or odd functions with respect to these planes. Thus, trial functions are classified in eight classes, so that each class is characterized by the parity of trial functions with respect to the coordinates x, y and z. In each class the parity in x, y and z of functions $v_1^{(3)}$, $v_2^{(3)}$ and θ coincides. Since the parity in x, y and z of functions $v_1^{(3)}$ and $v_2^{(3)}$ determines the parity of functions $v^{(1)}$ and $v^{(2)}$ respectively, the classification of trial functions is done in terms of the parity of θ. In the present work the following classification is used:

$$\begin{array}{llll} \text{class 1: OEE}, & \text{class 2: OOE}, & \text{class 3: EEE}, & \text{class 4: EOE}, \\ \text{class 5: OEO}, & \text{class 6: OOO}, & \text{class 7: EEO}, & \text{class 8: EOO}. \end{array} \tag{22}$$

The three letters of each class in expressions (22) refer to the parity (O=odd, E=even)[26] of the temperature θ with respect to the x, y and z axes, respectively.

As the parity of trial functions associated to each class determines which type of x–rolls and y–rolls is involved, the knowledge of the class associated to the critical eigenmode provides some preliminary information about the convective pattern near the bifurcation critical Rayleigh number. In cavities with square horizontal cross section, i.e., $h_1 = h_2$, classes 1 and 5 are respectively identical to classes 4 and 8. This leads to a multiplicity of the corresponding eigenvalues.

3.4 Transitions from the conductive state

The linear stability analysis of the Rayleigh-Bénard problem performed by Catton[21] in a cubical cavity showed that the smallest critical Rayleigh number is equal to $Ra_c = 3446$. At this critical value a single x– or y–roll structure develops. On the other hand, Pallarès et al.[16] reported five different convective steady structures; three roll structures named $S1$, $S2$ and $S3$, a toroidal structure named $S4$ and a four–roll structure named $S5$. These convective structures appear for values of $Ra < 10^4$ and were numerically obtained by adding to the initial steady conductive state a random disturbance of ± 0.05 in the temperature field and letting the system evolve in time. Structures $S1$ and $S2$ were also numerically predicted by Ozoe et al.[27], while the toroidal roll structure $S4$ was previously reported by Hernández and Frederick[22]. Therefore, the numerical calculations of Pallarès et al.[16] revealed that two additional critical Rayleigh numbers exist at $Ra_c \simeq$ 6000 and 7800. The existence of these three critical transitions previously reported in the literature[16,21,22,27] is confirmed when the complete set of trial functions given in subsection 3.3 is adopted, as shown in Table 1. There is reasonable agreement between the present critical Rayleigh numbers and the corresponding type of flow structure with those reported in the literature for $Ra < 10^4$, except for the additional critical transition to $S6$ detected at $Ra_c \simeq 8610$ by the current analysis. At this value an unstable steady solution bifurcates from another unstable solution. This explains why previous DNS results[16,21,22,27] have not detected the direct generation of $S6$ from the conductive state.

According to linear theory the Rayleigh number becomes a bifurcation point or a critical value Ra_c when M_l has a zero eigenvalue for any $l \in \{1, \ldots, 8\}$. Despite the fact that any structure generated at critical Rayleigh numbers beyond the first bifurcation should be initially unstable according to linear theory, they could become stable afterwards at secondary bifurcation points. Whenever the eigenvalue is simple the associated normalized eigenvector describes, qualitatively, the type of flow developed at the bifurcation point, i.e., the solution is close to a multiple of that eigenvector. The variation of several of the largest eigenvalues calculated from the linearized equations for the eight blocks with Ra is given in Figure 2. This figure shows that the eigenvalues associated to blocks M_5, M_6, M_7 and M_8 become positive only for $Ra > 2 \times 10^4$ and therefore they are not relevant to the linear stability analysis. Figure 2 also illustrates that one of the four critical Rayleigh numbers (or points of zero crossing) obtained for $Ra < 10^4$ is associated to block M_2 and, therefore, could not be determined using Catton's set. It should be mentioned that for the cubical cavity, and whenever $h_1 = h_2$, blocks M_1 and M_5 are equivalent to blocks M_4 and M_8, respectively, when x and y are exchanged and, therefore, their eigenvalues become multiple eigenvalues.

Table II shows the convergence of the critical Rayleigh numbers for the single roll ($S1$), the four rolls ($S5$), and the 2x-rolls + 2y-rolls ($S4$) as the number of trial functions is increased. The parameters N_x, N_y and N_z denote the number of trial functions used in the x, y and z direction, respectively. The total number of trial functions is given by $N = 3 \times N_x \times N_y \times N_z$. Convergence is satisfactory for the three prototypical structural topologies chosen for this test since the difference between $(3 \times 8 \times 8 \times 8)$ and $(3 \times 5 \times 5 \times 5)$ trial functions is always smaller than 0.13%. The results in Table II also indicate that an increase from $(3 \times 7 \times 7 \times 7)$ to $(3 \times 8 \times 8 \times 8)$ functions causes at most a 0.02% change in the critical value. One can even extrapolate the data in Table II to $N = \infty$ by using a law of the form $a + b/N$. The corresponding values for the three structures $S1$, $S5$ and $S4$ are 3388.6, 5900.5 and 7455.8, respectively. The differences between the $(3 \times 7 \times 7 \times 7)$ data and the extrapolated ones are below 0.06% in all cases. Therefore, all current results have been calculated with $(3 \times 7 \times 7 \times 7)$ functions.

The present study predicts that the smallest critical Rayleigh number is 3389, as shown in Table I. This critical value is an eigenvalue for both M_1 and M_4, indicating that any linear combination of the two eigenfunctions, i.e., of one x–roll and one y–roll, is possible according to linear stability analysis. Nevertheless, among all possible combinations, only a single x– or y–roll and a diagonal–roll are found when applying nonlinear theory (see next section), in agreement with the structures reported numerically and experimentally by Pallarès et al.[16,20]. The first structure, named $S1$ following the notation of these authors, is formed by one x–roll (or, by exchanging the roles of x and y, by one y–roll) while the second one, named $S2$, is also a single–roll but with a diagonal mode of circulation. This mode is obtained, in the linear approximation, by subtracting one x–roll from one y–roll. In a similar way, a symmetric solution is found by adding them.

At the second critical Rayleigh number of 5902 a four–rolls flow structure, named $S5$ (see[16] for the notation), is developed, as indicated in Table I. It is associated with the block M_2 and is formed by the sum of one x–roll and one y–roll, each one of them changing the sense of rotation at the two central orthogonal vertical planes of the cavity. This $Ra_c = 5902$ cannot be predicted by the incomplete set of functions previously proposed[21].

Structure $S4$ which develops at the third critical Rayleigh number of 7458 is associated to the block M_3 and has a toroidal configuration. The linear stability analysis shows that $S4$ is the sum of two x–rolls and two y–rolls with no change of rotation along their axes. A fifth structure $S6$, also associated with this block M_3, is predicted by the stability analysis at $Ra_c \approx 8610$. This structure, which corresponds to the subtraction of two x–

rolls and two y–rolls, has not been found by finite difference calculations near its critical Rayleigh[16]. Pallarès et al.[20] observed $S6$ in experiments carried out in a cubical cavity with conducting lateral walls at $Pr = 130$ and also at much higher Rayleigh numbers ($Ra \geq 1.2 \times 10^5$).

The current linear analysis also includes the study of the effect of changing the aspects ratios depth/height and length/height (h_2, h_1) on the bifurcation Rayleigh numbers for parallelepipedic cavities. Considering the fact that $Ra_c(h_1, h_2) = Ra_c(h_2, h_1)$ the coordinates x and y can be exchanged and, thus, the bifurcation Rayleigh numbers can be estimated as a function of either h_2 or h_1. Figure 3 shows the variation of the bifurcation Rayleigh number with h_2 for $h_1 = 0.5$, 1 and 2 over the range $0.5 \leq h_2 \leq 4.5$. The curves obtained by choosing the lowest bifurcation Rayleigh number present breaks at several values of h_2, as reported by Davis[23], indicating transitions between the different possible structures. The type of flow developed along any of the bifurcation curves shown in Figure 3 has been determined studying how the main modes of the associated normalized eigenvectors change continuously as a function of h_2. Transitions associated with blocks M_3 and M_4 differ from those reported by Davis[23]. The different curves for each k–number of y–rolls reported by this author would contradict the continuous and even analytical (except when the eigenvalue has multiplicity greater than 1) variation of the eigenvector with respect to the parameter h_2 reported here.

4 Bifurcated branches ant their stability

4.1 Numerical method

Linear stability analysis cannot determine which kind of flow will develop when the critical Ra_c is a multiple eigenvalue, such as it happens when two bifurcation curves intersect, because any linear combination of the independent eigenvectors is possible. To determine which one of these combinations occurs in such situations, i.e., whenever the minimum critical Rayleigh number curve presents a break, it is necessary to carry out a non–linear analysis of the flow. Precisely, the first break in the curve plotted in Figure 3 for $h_1 = 1$ corresponds to the cubical case. A non–linear analysis is also needed to determine whether any structure that appears at a critical Rayleigh number beyond the first one, and that is initially unstable according to the linear theory, becomes stable because of a new bifurcation afterwards ($Ra > Ra_c$).

The method consists first in expanding and truncating any solution of the nonlinear equations (1–3) in series of eigenvectors of the linear problem

$$\vec{a}(t, x, y, z) = \sum_{l=1}^{L} a(l) \vec{F}_l(x, y, z), \tag{23}$$

where $a(l)$ denotes a function of t. The eigenvectors $\vec{F}_l$ used in the present work are those of the matrix $M(Ra_0)$ defined in (12), where Ra_0 is a Rayleigh number close to a critical one. Eigenvectors belonging to each block $M_i(Ra_0)$ are ordered by decreasing eigenvalue. The results reported have been computed using the eigenvectors F_l obtained for $(7 \times 7 \times 7)$ trial functions and $L = 250$.

The nonlinear problem considered is reduced to a system of ordinary differential equations after applying the Galerkin method. Thus, the powerful and well–established theory and numerical methods for ordinary differential equations will be applied both to obtain stationary solutions and to study the stability of solutions. The system of ordinary differential equations may be written as

$$\sum_{i=1}^{L} b(i,j)a'(i) = \sum_{i=1}^{L}(l_1(i,j)+rl_2(i,j))a(i)-\frac{r}{2}\sum_{i=1}^{L}\sum_{n=1}^{L} q(i,n,j)a(i)a(n),\ \ j=1,\ldots,L\,, \quad (24)$$

where $r = Ra^{\frac{1}{2}}$ and

$$b(i,j)=\begin{pmatrix}\frac{1}{Pr}F_i^{(1)}\\ \frac{1}{Pr}F_i^{(2)}\\ \frac{1}{Pr}F_i^{(3)}\\ F_i^{(4)}\end{pmatrix}\bullet\begin{pmatrix}F_j^{(1)}\\ F_j^{(2)}\\ F_j^{(3)}\\ F_j^{(4)}\end{pmatrix},\ l_1(i,j)=\begin{pmatrix}\nabla^2F_i^{(1)}\\ \nabla^2F_i^{(2)}\\ \nabla^2F_i^{(3)}\\ \nabla^2F_i^{(4)}\end{pmatrix}\bullet\begin{pmatrix}F_j^{(1)}\\ F_j^{(2)}\\ F_j^{(3)}\\ F_j^{(4)}\end{pmatrix},\ l_2(i,j)=\begin{pmatrix}0\\ 0\\ F_i^{(3)}\\ F_i^{(4)}\end{pmatrix}\bullet\begin{pmatrix}F_j^{(1)}\\ F_j^{(2)}\\ F_j^{(3)}\\ F_j^{(4)}\end{pmatrix}, \quad (25)$$

$$q(i,n,j)=\begin{pmatrix}\frac{1}{Pr}\sum_{r=1}^{3}F_i^{(r)}D_rF_n^{(1)}\\ \frac{1}{Pr}\sum_{r=1}^{3}F_i^{(r)}D_rF_n^{(2)}\\ \frac{1}{Pr}\sum_{r=1}^{3}F_i^{(r)}D_rF_n^{(3)}\\ \sum_{r=1}^{3}F_i^{(r)}D_rF_n^{(4)}\end{pmatrix}\bullet\begin{pmatrix}F_j^{(1)}\\ F_j^{(2)}\\ F_j^{(3)}\\ F_j^{(4)}\end{pmatrix}+\begin{pmatrix}\frac{1}{Pr}\sum_{r=1}^{3}F_n^{(r)}D_rF_i^{(1)}\\ \frac{1}{Pr}\sum_{r=1}^{3}F_n^{(r)}D_rF_i^{(2)}\\ \frac{1}{Pr}\sum_{r=1}^{3}F_n^{(r)}D_rF_i^{(3)}\\ \sum_{r=1}^{3}F_n^{(r)}D_rF_i^{(4)}\end{pmatrix}\bullet\begin{pmatrix}F_j^{(1)}\\ F_j^{(2)}\\ F_j^{(3)}\\ F_j^{(4)}\end{pmatrix}. \quad (26)$$

The prime in equation (24) means differentiation with respect to time. If $nb(i)$ denotes the block associated to the trial function F_i, the coefficients of equation (24) verify,

$$\begin{aligned}\left\{\begin{array}{c} l_1(i,j)\neq 0\\ l_2(i,j)\neq 0\end{array}\right\} &\iff nb(i)=nb(j)\,,\\ q(i,n,j)\neq 0 \quad &\iff (nb(i),nb(n),nb(j))\in\mathcal{S}\,,\end{aligned} \quad (27)$$

where $\mathcal{S} = \{\ \wp(1,2,8),\ \wp(1,3,5),\ \wp(1,4,6),\ \wp(2,3,6),\ \wp(2,4,5),\ \wp(3,4,8),\ \wp(5,6,8)\ \}$ $\cup\,(\cup_{j=1,\ldots,8}\{\wp(j,j,7)\})$ and $\wp(i,j,k)$ denotes the group of permutations of three elements.

The current procedure applied first the Newton's method to calculate stationary solutions of the nonlinear equation (24) for values Ra_0 close to critical ones. The Newton's procedure was initiated with approximate solutions obtained by standard bifurcation analysis[28]. Then a path-continuation method based on a modified Newton's method[28] was used to compute stationary solutions of the nonlinear equation (24) with Ra as a continuation parameter. Along the solution branches the stability properties were checked so that new bifurcations were identified. It should be mentioned that this procedure yielded stationary solutions of (24) that belong either to the subspace generated by the basis functions associated to a pair of blocks (M_7 and any other) or to four blocks (M_6, M_7 and either M_1, M_4 or M_5, M_8). However, functions of all classes should be used to characterize the stability along the solution branches and to identify new bifurcations.

A given steady solution $\vec{a}^e$ of (24) is unstable if the matrix

$$B^{-1}\, Dg(\vec{a}^e) \tag{28}$$

has at least one eigenvalue λ with positive real part, and it is asymptotically stable if all eigenvalues have negative real parts. In equation (28) B and $Dg(\vec{a}^e)$ are $L \times L$ matrices defined as

$$\begin{aligned} B(i,j) &= -b(i,j), \\ Dg(i,j) &= -l_1(j,i) + Ra^{\frac{1}{2}} \left(-l_2(j,i) + \sum_{l=1}^{L} q(j,l,i) a^e(l) \right), \end{aligned} \tag{29}$$

with b, l_1, l_2 and q defined respectively by expressions (25) and (26). Both b and q depend on Prandtl's number. This eigenvalue problem, associated with stability analysis of the non-linear stationary solutions along the bifurcated branches, has been solved using the QR algorithm. Whenever the real part of an eigenvalue of the matrix $B^{-1}\, Dg(\vec{a}^e)$ changes sign (crosses zero), the associated Rayleigh number becomes a new bifurcation point, and new convective structures appear. These structures have also been examined but are not explicitly reported here since all of them are unstable for values of Ra up to 7×10^4.

4.2 Bifurcation diagram

The bifurcation diagram at $Pr = 0.71$ is depicted in Figure 4. The branches of this diagram were obtained by solving the non-linear stationary counterpart of the governing equations given in section 2. The stability of the flow along the branches was determined by solving the eigenvalue problem of the linearized equations around each point. In this figure the variation of the absolute value of the principal component for all flow structures identified is plotted as a function of Ra. Since the dominant component can change with Ra, these changes are indicated with broken lines in the plot. Stable and unstable structures are represented by continuous and discontinuous lines, respectively. Bifurcation points are marked with dots and identified by capital letters. Flow structures that originate when $S4$, $S5$ and $S6$ bifurcate are identified with the addition of a and b in their respective notation. Note also that the branch $S4a$ emerging from $S4$ at B coincides with the branch $S6a$ ending at $S6$ in D.

Figure 4 indicates that $S1$ and $S5$ are stable, according to the variation with Ra of the real parts of the principal eigenvalues of the matrix $B^{-1}\, Dg(\vec{a}^e))$ depicted in Figure 5 for both structures at $Pr = 0.71$ and 130. The real part of the principal eigenvalues for $S1$ are negative over the whole range of Ra considered ($Ra_c \simeq 3389 \leq Ra \leq 7 \times 10^4$) for both Prandtl numbers, indicating that this single-roll structure is always stable. This figure 5 also shows that $S5$ is unstable when it originates at $Ra_c \simeq 5902$ since it has a positive double eigenvalue. This initial instability of $S5$ is consistent with linear theory because it appears beyond the first critical transition $Ra_c \simeq 3389$. The double positive eigenvalue of $S5$ becomes negative at $Ra \approx 8900$ and $Ra \approx 10400$ for $Pr = 0.71$ and 130, respectively, and, thus, $S5$ becomes stable at these conditions and remains so thereafter. Figure 4 shows that two additional structures $S5a$ and $S5b$ develop at this bifurcation point A ($Ra \approx 8900$) for $Pr = 0.71$. Both structures are unstable for values of Ra up to 7×10^4 at $Pr = 0.71$ and 130, as shown in Figure 6. There is a Hopf bifurcation associated to structure $S5a$ for $Pr = 0.71$, which is identified with the letter H in Figure 4. However, the non–stationary flow structures with periodic orbits that appear at this point H have not been studied in the current work.

Figure 7 shows that structures $S2$, $S4$, and $S6$ have at least one positive principal eigenvalue for values of Ra up to 7×10^4 at $Pr = 0.71$ and 130 and, thus, are unstable. Structure $S2$ is the less unstable of the three since its only positive eigenvalue remains close to zero near the Ra_c at both Prandtl numbers. This explains why a relatively small numerical diffusion caused by the use of coarse grids in direct numerical simulations of the flow[16] could be sufficient to stabilize $S2$. When this diffusion was reduced and the numerical calculations were carried out over a sufficiently large time interval for the perturbations to grow, this diagonal–roll first reported by Pallarès et al.[16] evolved into the stable $S1$–roll[20]. It should be noted that new bifurcations for $S4$ and $S6$ take place at points B, C and D where the real part of their eigenvalues changes sign, as can be observed in Figure 7. These zero crossings for both structures at $Pr = 0.71$ correspond to the bifurcations identified in the diagram of Figure 4.

The only structures found by Pallarès et al.[20] in visualization and PIV experiments carried out at $Pr = 130$ with silicon oil are the stable structures $S1$, $S5$, the slightly unstable structure $S2$ and a structure named $S7$. The fact that this unstable structure

$S2$ is found experimentally for Rayleigh numbers up to 10^4 may be due to the impossibility of implementing experimentally a perfect cubical geometry with perfect adiabatic lateral walls, particularly at the four vertical edges. These imperfections seem sufficient to stabilize $S2$ at low Rayleigh numbers, when the only positive eigenvalue in Figure 7b is close to zero. On the other hand, structure $S7$ may be considered a single–roll because the projection of its numerical velocity and temperature fields at $Ra = 5 \times 10^4$ and $Pr = 130$ onto the space generated by the basis functions yields a structure which is very similar to $S1$. In fact it differs from $S1$ just because it has components, the greatest of the order of 10^{-2}, onto the space generated by the trial functions associated to blocks M_3 and M_6. A modified Newton's method converges to $S1$ when this projection is taken as initial condition. Pallarès et al.[20] could only identify structure $S4$, which is unstable according to the current study (see Figure 7), during the unsteady start-up transition from the conductive state towards $S1$ at $Pr = 130$. Furthermore, the effects of perturbations caused by slightly changing the aspect ratio or tilting the cavity confirm[16] the unstable character of $S2$, $S4$ and $S6$. Therefore, there is good agreement between the present study with the complete set of basis functions and previous experimental and numerical results.

Figures 8, 9 and 10 depict, respectively, the isocontours of the vertical velocity and temperature fields of the stable structures $S1$ and $S5$, and the nearly stable $S2$ at $z = 0$, in the proximity of their critical Rayleigh at $Pr = 0.71$. A detailed 3D visualization of these structures can be found elsewhere[16,20]. Figure 8 shows the single–roll characteristic motion of $S1$, with symmetrical ascending and descending motions at the horizontal midplane. There is quantitative agreement between the isocontours predicted numerically[16] and by the current non–linear analysis, while the linear analysis predictions are qualitatively correct but deviate slightly. Similar results are observed in Figures 9 and 10 where the ascending and descending motions that define the four–rolls of $S5$ and the diagonal–roll of $S2$ are shown, respectively. Again, there is agreement between the present non–linear stability analysis and previous finite difference calculations[16]. The linear stability analysis is also sufficient to describe qualitatively the type of flow structure that develops near the critical Rayleigh, but differences increase with Ra. The vertical velocity contours associated to flow structures $S1$, $S2$, $S4$, $S5$ and $S6$ at the highest Rayleigh studied, $Ra = 7 \times 10^4$, are summarized in Figure 11. These vertical velocity isocontours are in agreement with numerical predictions reported in the literature[16]. They also confirm the tendency of the vertical velocity associated to the structure $S1$ to develop two maxima and two minima at the horizontal midplane $z = 0$ when the Rayleigh number increases from the critical value. The remaining flow structures do not change their topology with increasing Rayleigh number, as can be observed for $S5$ and $S2$ by comparing Figures 9 and 10 with Figure 11.

To evaluate quantitatively the agreement between the direct numerical simulation results and the velocity patterns of $S1$ and $S5$ resulting from the stability analysis shown in Figures 8 and 9, the numerical data were projected onto the corresponding subspace generated by the basis functions. This projection was carried out using the least-squares method and taking 250 trial functions, 125 in each of the two blocks associated to the structure. The choice was made according to the relevance of the eigenvalue. The components of the projections together with the components predicted by stability analysis are depicted in Figure 12. The projections in Figure 12 show an excellent agreement at $Ra = 10^4$ while small discrepancies appear near the Ra_c. These differences could be due to the difficulty in ascertaining when a non-stationary direct numerical calculation is close enough to a stationary solution. This difficulty increases when the critical value has to be predicted by DNS. Indeed, close to a bifurcation, the dominant eigenvalue of a stable stationary solution is very close to zero. Hence the direct numerical calculation converges very slowly to the stationary solution, especially if extrapolation is not used.

Figure 13 depicts the variation with Ra of the real part of the principal eigenvalues associated to flow structures $S4a$, $S4b$ and $S6a$ that develop when $S4$ and $S6$ bifurcate (points B, C and D in Figure 4). Figure 13 shows that all these flow structures are unstable for values of Ra up to 7×10^4 as they have eigenvalues with a positive real part. It should be noted that at $Pr = 0.71$ structure $S4a$, which appears as a supercritical bifurcation of $S4$, coincides with structure $S6a$ which is found as a subcritical bifurcation of $S6$. The fact that this phenomenon takes place at $Pr = 0.71$ but has not been observed at $Pr = 130$ would explain the reversible transition from $S4$ to $S6$ over $10^4 \leq Ra \leq 1.5 \times 10^4$ reported by Pallarès et al.[16] at $Pr = 0.71$. Figure 14 displays the development of structure $S4a$ ($= S6a$) at $Pr = 0.71$ and shows that this unstable structure is very similar to $S4$ near its supercritical Rayleigh ($Ra \approx 11668$) and becomes very similar to $S6$ near its subcritical Rayleigh ($Ra \approx 34830$). Its topology at $Ra = 2 \times 10^4$ is in good agreement with the numerical results of Pallarès[16] for their reported $S6$. In fact Pallarès et al.[16] do not distinguish $S6$ from $S6a$.

5 Conclusions

The solutions of the stationary equations for velocity and temperature, obtained with a Galerkin method by using a complete set of divergent–free basis functions, identify four bifurcations from the conductive state at critical Rayleigh numbers $Ra_c \simeq 3389$, 5902, 7458 and 8610. At the first transition from the conductive state a x–roll and a diagonal–roll (x–roll $\pm$ y–roll) are formed. While the former is stable over the whole range of Ra studied ($Ra < 7 \times 10^4$) the latter is slightly unstable, with instability increasing with Rayleigh number. The single–roll structure has been identified numerically and experimentally [16,20] over a wide range of Rayleigh numbers while the diagonal–roll was also observed near the critical value. This discrepancy in the stability of the diagonal–roll may be attributable to the stabilization caused by numerical diffusion in the finite volume calculations and by deviations in the adiabatic conditions at the four lateral walls in the experiments, particularly near the vertical edges of the cavity.

The second bifurcation at $Ra \simeq 5902$ yields a four–rolls structure (x–roll + y–roll with both rolls changing sense of rotation at the two central orthogonal vertical planes). This initially unstable four–rolls structure stabilizes beyond $Ra = 8900$ and $Ra \approx 10400$ at $Pr = 0.71$ and $Pr = 130$, respectively, in agreement with previous numerical and experimental results. Thus, the results presented explain the stabilization of the experimentally observed[20] four-roll structure beyond the transition from the conductive state region where it appears as an unstable structure. Flow structures which appear at this new bifurcation in addition to $S5$ turn out to be unstable over the whole range of Ra considered.

At $Ra \simeq 7458$ a highly unstable $2x$–rolls + $2y$–rolls structure is formed while a $2x$–rolls − $2y$–rolls develops at $Ra = 8610$. Both structures were also identified numerically by Pallarès et al.[16] but were destabilized by small perturbations caused by changes in geometry and tilting of the cavity.

The linear stability analysis of the effect of changing the aspect ratios of the cubical cavity on the bifurcation Rayleigh numbers shows that there is a continuous evolution of the flow towards multiple single–roll configurations as the cavity elongates, with the axis of rotation parallel to the shortest side. These results are in agreement with other incomplete linear stability studies reported in the literature.

Acknowledgments

D.P., F.X.G. and F.G. acknowledge the financial support received from Spain, DGICYT projects PB96-1011 and PPQ2000-1339, and from Catalunya, CIRIT grants 1998SGR-00102 and 2000SGR-00103. C.S. has been partially supported by the Spanish grant, BFM2000-805 and the Catalan grants CIRIT 1998SGR-42 and 2000SGR-27.

References

[1] E.L. Koschmieder 1993 *Bénard Cells and Taylor Vortices.* Cambridge Monographs on Mechanics and Applied Mathematics. Cambridge University Press. Cambridge.

[2] A.V. Getling 1998 *Rayleigh-Bénard convection: structures and dynamics.* Advanced Series in Nonlinear Dynamics, 11. World Scientific Publishing.

[3] De Vahl Davis 1983 *Natural convection of air in a square cavity: a benchmark numerical solution.* Int. J. for Numer. Meth. in fluids, 3, 249–264.

[4] A.Y. Gelfgat, 1999 *Different modes of Rayleigh–Bénard instability in two and three dimensional rectangular enclosures.* J. Comput. Physics,156, 300–324.

[5] H.A. Dijkstra 1988 *Test problem: Rayleigh–Bénard convection. http://www.euromech.cz/Text/finalr98.phtml#383.*

[6] S. Albensoder, H.C. Kuhlmann and H.J. Rath 2001 *Three–dimensional centrifugal–flow instabilities in the lid–driven–cavity problem.* Phys Fluids., 13, 121–135.

[7] M.P. Dyko, K. Vafai and A.K. Mojtabi 1999 *A numerical and experimental investigation of stability of natural convective flows within an horizontal annulus.* J. Fluid Mech., 381, 27–61.

[8] S. Kenjeres and K. Hanjalic 1999 *Transient analysis of Rayleigh–Bénard convection with RANS model.* Int. J. Heat and Fluid Flow., 20, 329–340.

[9] A.Y. Gelfgat, P.Z. Bar-Yoseph and A.L. Yarim 1999 *Stability of multiple steady states of convection in laterally heated cavities.* J. Fluid Mech., 388, 315–334.

[10] F. H. Busse, R. M. Clever 1979 *Instabilities of convection rolls in a fluid of moderate*

Prandtl number. J. Fluid Mech., 91, 319–335.

[11] R. M. Clever, F. H. Busse 1974 *Transition to time–dependent convection.* J. Fluid Mech., 65, 625–645.

[12] I. Catton 1988 *Wavenumber selection in Bénard convection.* Transactions of the ASME, 110,1154–1165.

[13] R.A.W.M. Henkes, P. LE Quéré 1996 *Three–dimensional transition of natural–convection flows.* J. Fluid Mech., 319, 281-303.

[14] R. Kessler 1987 *Nonlinear transition in three–dimensional convection.* J. Fluid Mech., 174, 357-379.

[15] J. Humphrey, J. Cushner, Sudarsan R., M. Al-Shannag, J. Herrero, F. Giralt 2001 *Experimental and numerical investigation of the shear-driven flow in a toroid of square cross-section.* Second International Symposium on Turbulence and Shear Flow Phenomena, Stockholm, Sweden, June 27-28.

[16] J. Pallarès, F.X. Grau, F. Giralt 1999 *Flow transitions in laminar Rayleigh-Bénard convection in a cubical cavity at moderate Rayleigh numbers.* Int. J. Heat Mass Transfer, 42, 753–769.

[17] R.J.A. Janssen and R.A.W.M. Henkes 1996 *Instabilities in three–dimensional differentially–heated cavities with adiabatic horizontal walls.* Phys Fluids., 8, 62–.

[18] K.H. Winters, K.A. Cliffe and C.P. Jackson 1987 *The prediction of instabilities using bifurcation theory.* Num. Methods for Transient and Coupled problems. 179-198

[19] A.Y. Gelfgat, I. Tanasawa 1994 *Numerical analysis of oscillatory instability of buoyancy*

convection with the Galerkin spectral method. Numerical Heat Transfer. Part A, 25, 627–648

[20] J. Pallarès, M.P. Arroyo, F.X. Grau and F. Giralt 2001 *Experimental laminar Rayleigh-Bénard convection in a cubical cavity at moderate Rayleigh and Prandtl numbers.* Experiments in Fluids. In press.

[21] I. Catton 1972 *The effect of insulating vertical walls on the onset of motion in a fluid heated from below.* Int. J. Heat Mass Transfer, 15, 665–672.

[22] R. Hernández, R.L. Frederick 1994 *Spatial and thermal features of three dimensional Rayleigh-Bénard convection.* Int. J. Heat Mass Transfer, 37, 411–424.

[23] S.H. Davis 1967 *Convection in a box: linear theory.* J. Fluid Mech., 30, 465–478.

[24] M. Sherman, S. Ostrach 1966 *On the principle of exchange of stabilities for the magneto-hydrodynamic thermal stability problem in completely confined fluids.* J. Fluid Mechanics, 24, 661–671.

[25] C. Canuto, M.Y. Hussaini, A. Quarteroni, T.A. Zang 1987 *Spectral Methods in Fluid Dynamics.* Springer Series in Computational Physics. Springer Verlag. New York.

[26] P.C. Dauby and G. Lebon 1996 *Bénard–Marangoni instability in rigid rectangular containers.* J. Fluid Mechanics, 329, 25–64.

[27] H. Ozoe, K. Yamamoto, S.W. Churchill, H. Sayama 1976 *Three–dimensional numerical analysis of laminar natural convection in a confined fluid heated from below.* ASME J. Heat Transfer, 98,202–207.

[28] C. Simó 1990 *Analytical and numerical computation of invariant manifolds.* In D. Ben-

est et C. Froeschlé, editors, *Modern methods in celestial mechanics*, 285–330, Editions Frontières, Paris.

Table I: Critical Rayleigh numbers and type of flow structure developed at the bifurcations from the conductive state in a cubical enclosure.

Type of structure	**Catton** (1972)	**Hernandez** (1994)	**Pallarès et al.** (1999)	**Present work**
x–roll ($S1$)	3446	–	3500	3389
diagonal–roll ($S2$)	–	–	3500	3389
four–rolls ($S5$)	–	–	6000	5902
$2x$–rolls + $2y$–rolls ($S4$)	–	8000	7800	7458
$2x$–rolls − $2y$–rolls ($S6$)	–	–	–	8610

Table II: Convergence of the critical Rayleigh numbers as a function of the number of trial functions ($N = 3 \times N_x \times N_y \times N_z$) used. The last column includes the relative differences between $3 \times 8 \times 8 \times 8$ and $3 \times 7 \times 7 \times 7$ trial functions.

Type of structure	$3\times5\times5\times5$	$3\times6\times6\times6$	$3\times7\times7\times7$	$3\times8\times8\times8$	$\Delta_{8-7}\%$
x–roll ($S1$)	3391.17	3390.09	3389.53	3389.21	0.0094
four–rolls ($S5$)	5910.09	5906.03	5903.97	5902.81	0.0197
$2x$–rolls + $2y$–rolls ($S4$)	7462.98	7459.79	7458.35	7457.59	0.0102

Figure captions

Figure 1. Coordinate system of the cubical domain Ω.

Figure 2. Several of the largest eigenvalues of M_l, $1 \leq l \leq 8$, as a function of Ra for the cubical cavity.

Figure 3. Bifurcation Rayleigh numbers as a function of the aspect ratio h_2. (a) $h_1 = 0.5$; (b) $h_1 = 1$; (c) $h_1 = 2$. For $h_1 = 0.5$ and $h_1 = 2$ the critical value is associated to blocs M_3 or M_4. The block M_1 also appears for $h_1 = 1$.

Figure 4. Bifurcation diagram for $Pr = 0.71$. The component with greatest absolute value is depicted for all flow structures identified as a function of Ra. Continuous and discontinuous lines refer to stable and unstable structures, respectively. Bifurcation points are marked with dots and capital letters A, B, C, D and H.

Figure 5. Variation of the real part of the principal eigenvalues for the stable structures $S1$ (dashed lines) and $S5$ (solid lines) as a function of Ra: (a) $Pr = 0.71$; (b) $Pr = 130$.

Figure 6. Variation of the real part of the principal eigenvalues for the unstable structures $S5a$ (solid lines) and $S5b$ (dashed lines) as a function of Ra: (a) $Pr = 0.71$; (b) $Pr = 130$.

Figure 7. Variation of the real part of the principal eigenvalues for the unstable structures $S2$ (dashed lines), $S4$ (dash-point lines) and $S6$ (solid lines) as a function of Ra: (a) $Pr = 0.71$; (b) $Pr = 130$.

Figure 8. Vertical velocity contours (a1 to a3) and temperature contours (b1 to b3) in the horizontal midplane $z = 0$ for structure $S1$ at $Pr = 0.71$. Figures (a1-b1) and (a2-b2) show the contours predicted numerically by Pallarès et al.[16] and by non–linear stability

analysis at $Ra = 3500$. The contours predicted by linear stability analysis at $Ra_c = 3389$ are depicted in figures (a3-b3). Continuous and discontinuous lines refer to positive and negative values, respectively. The same convention has been used in the following Figures.

Figure 9. Vertical velocity contours (a1 to a3) and temperature contours (b1 to b3) in the horizontal midplane $z = 0$ for the structure $S5$ at $Pr = 0.71$. Figures (a1-b1) and (a2-b2) show the contours predicted numerically by Pallarès et al.[16] and by non–linear stability analysis at $Ra = 6500$. The contours predicted by linear stability analysis at $Ra_c = 5902$ are depicted in figures (a3-b3).

Figure 10. Vertical velocity contours (a1 to a3) and temperature contours (b1 to b3) in the horizontal midplane $z = 0$ for the structure $S2$ at $Pr = 0.71$. Figures (a1-b1) and (a2-b2) show the contours predicted numerically by Pallarès et al.[16] and by non–linear stability analysis at $Ra = 3500$. The contours predicted by linear stability analysis at $Ra_c = 3389$ are depicted in figures (a3-b3).

Figure 11. Vertical velocity contours in the horizontal midplane $z = 0$ predicted by non–linear stability analysis at $Ra = 70000$ and $Pr = 0.71$. (a) Structure $S1$; (b) structure $S2$; (c) structure $S4$; (d) structure $S5$; (e) structure $S6$.

Figure 12. Components of the projections of the stable flow structures predicted numerically onto the subspace generated by the trial functions at $Pr = 0.71$. (a1) Structure $S1$ at $Ra = 3500$; (a2) structure $S1$ at $Ra = 10^4$; (b1) structure $S5$ at $Ra = 6500$; (a2) structure $S5$ at $Ra = 10^4$. The index j indicates the number of the component. Only components larger than 10^{-3} times the greatest component have been considered.

Figure 13. Variation of the real part of principal eigenvalues as a function of Ra for the

unstable structures $S4a$ (solid lines), $S4b$ (dashed lines) and $S6a$ (dash-point lines). (a) $Pr = 0.71$; (b) $Pr = 130$. It should be noted that $S4a$ and $S6a$ coincide at $Pr = 0.71$.

Figure 14. Vertical velocity contours contours in the horizontal midplane $z = 0$ for structure $S4a$ (=$S6a$) at $Pr = 0.71$. (a) Contours predicted numerically by Pallarès et al.[16]; (b1 to b4) contours predicted by non–linear stability analysis.

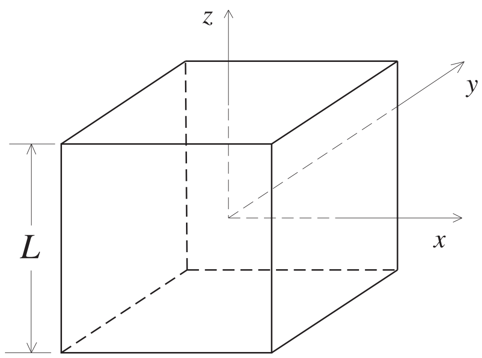

Figure 1: Coordinate system of the cubical region Ω.

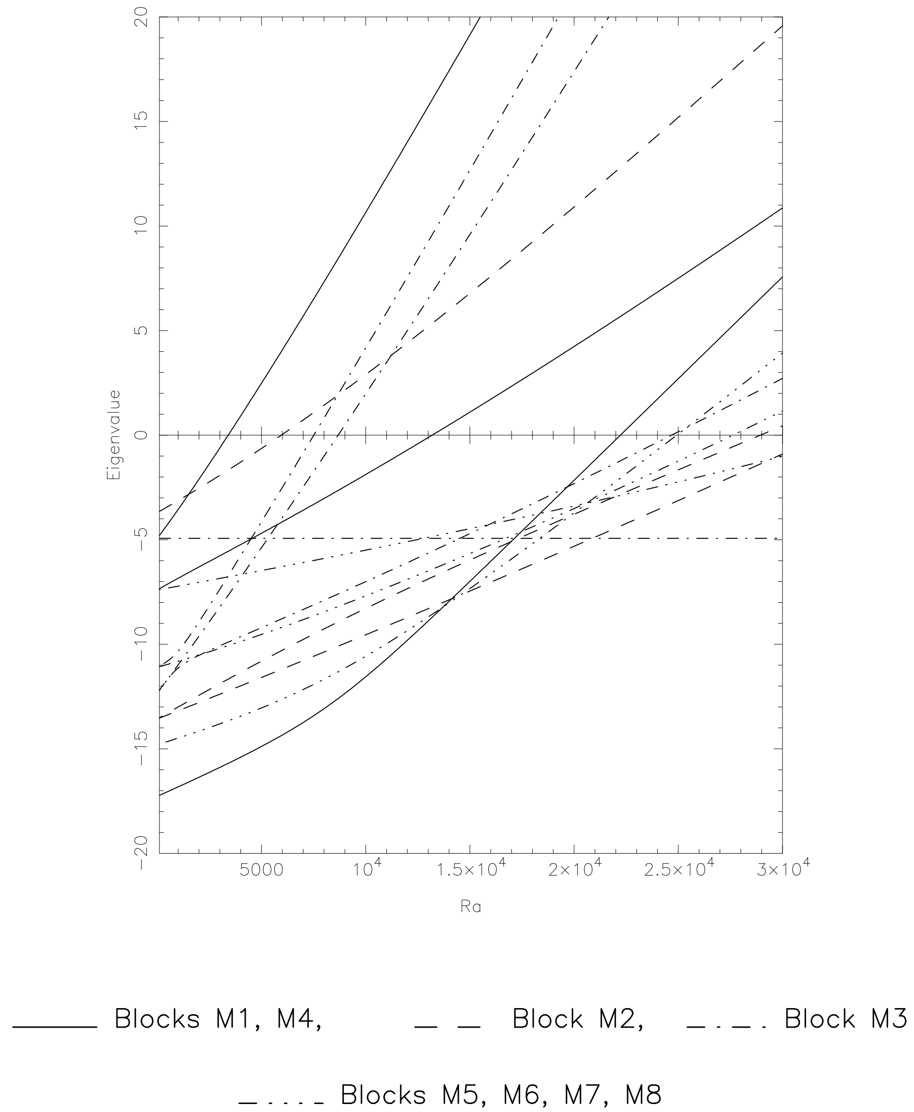

Figure 2: Several of the largest eigenvalues of M_l $1 \leq l \leq 8$ as a function of Ra for the cubical cavity.

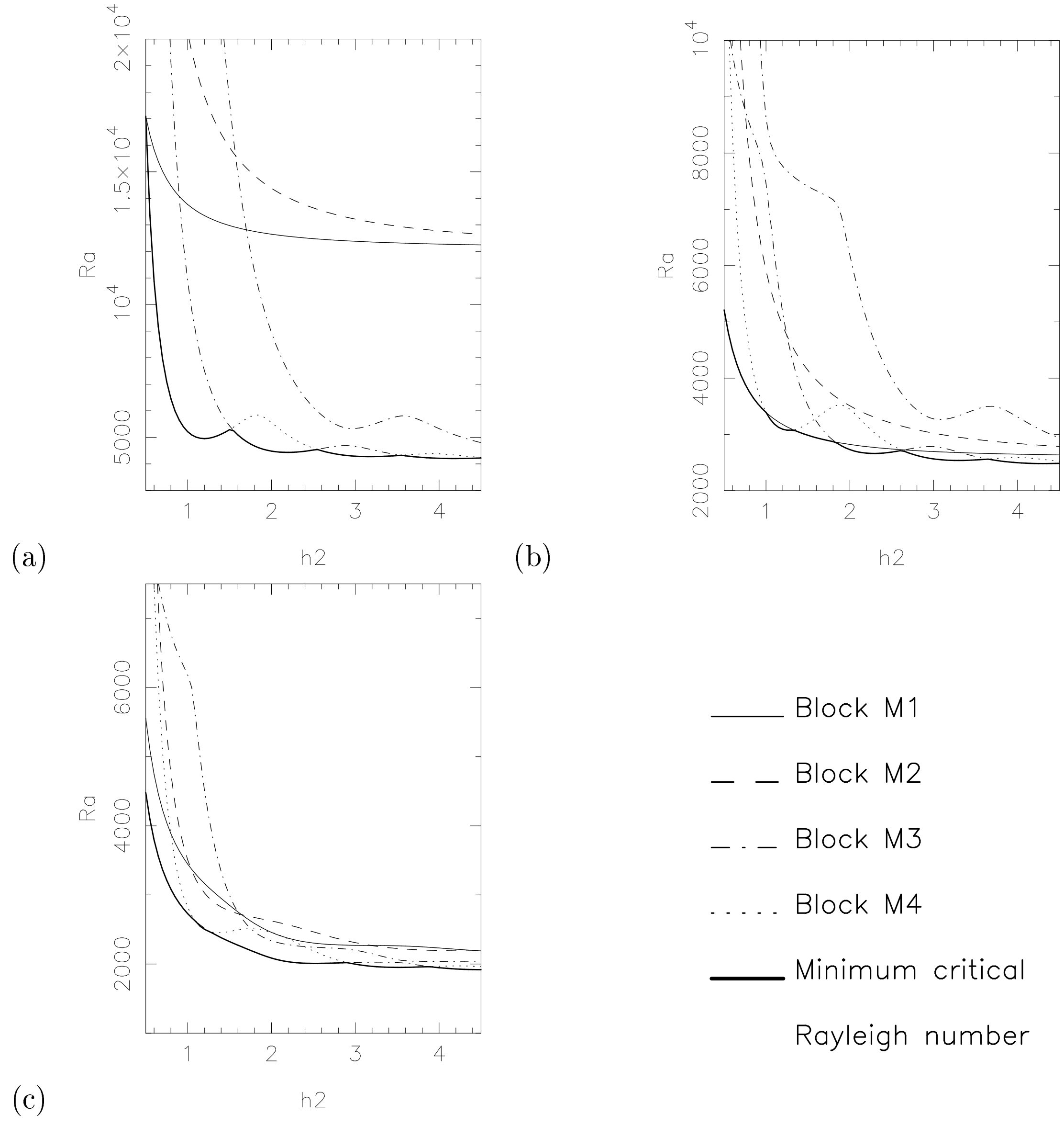

Figure 3: Bifurcation Rayleigh numbers as a function of the aspect ratio h_2. (a) $h_1 = 0.5$; (b) $h_1 = 1$; (c) $h_1 = 2$. For $h_1 = 0.5$ and $h_1 = 2$ the critical value is associated to blocs M_3 or M_4. The block M_1 also appears for $h_1 = 1$.

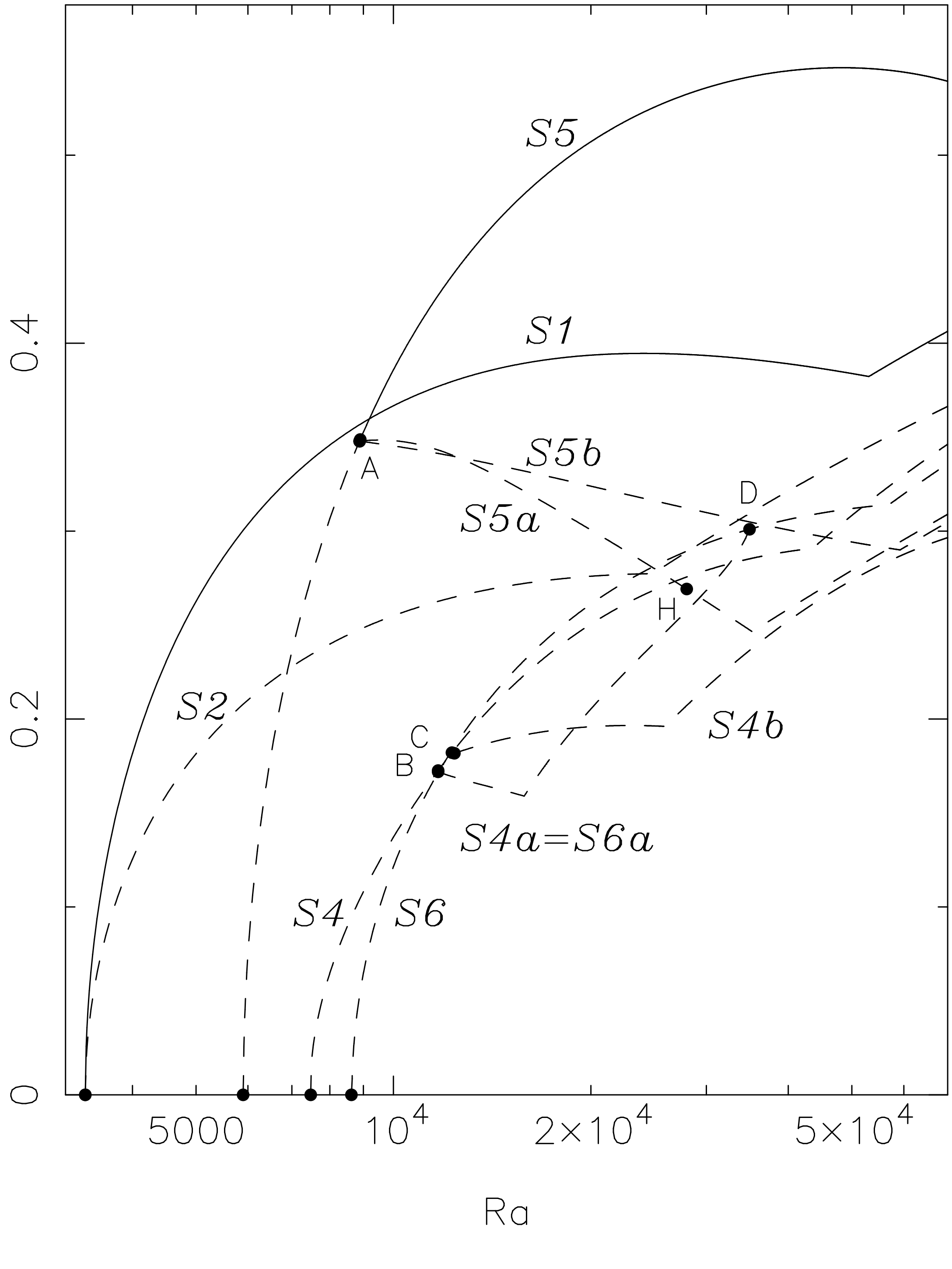

Figure 4: Bifurcation diagram at $Pr = 0.71$. The component with greatest absolute value is depicted for all flow structures identified as a function of Ra. Continuous and discontinuous lines refer to stable and unstable structures, respectively. Bifurcation points are marked with dots and capital letters A, B, C, D and H.

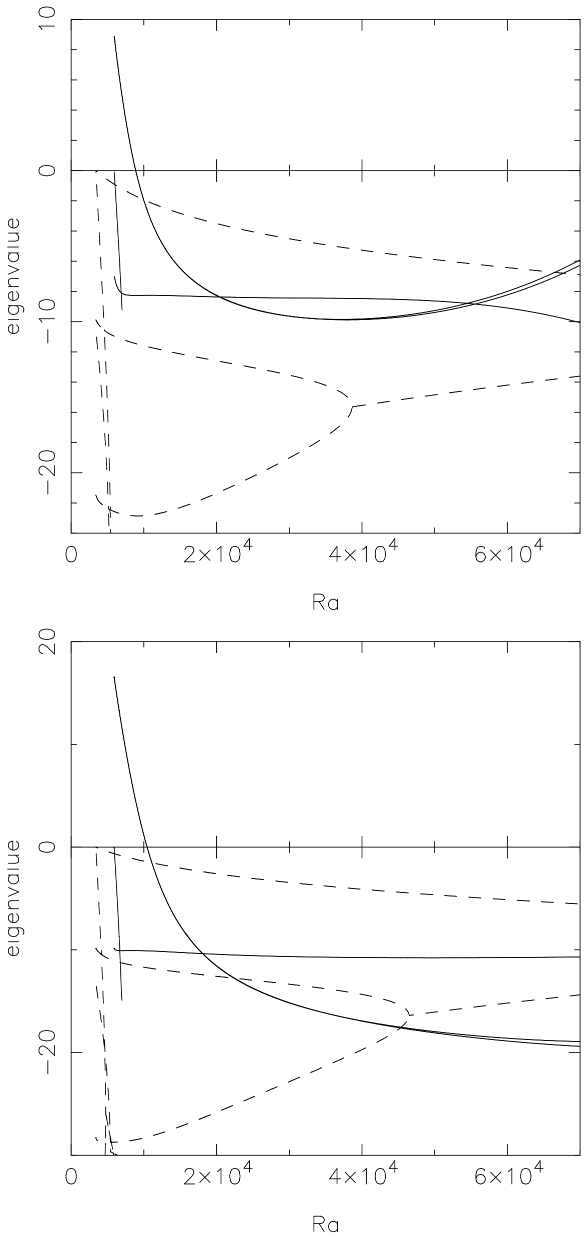

(a)

(b)

Figure 5: Variation of the real part of the principal eigenvalues for stable structures $S1$ (dashed lines) and $S5$ (solid lines) as a function of Ra: (a) $Pr = 0.71$; (b) $Pr = 130$.

(a)

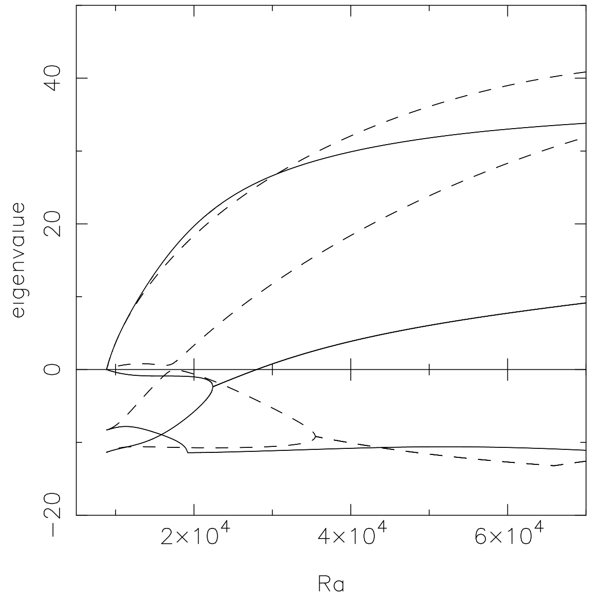

(b)

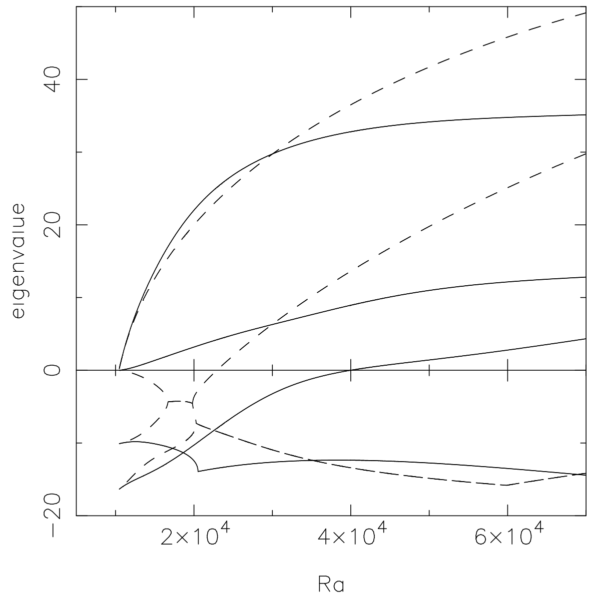

Figure 6: Variation of the real part of the principal eigenvalues for unstable structures $S5a$ (solid lines) and $S5b$ (dashed lines) as a function of Ra: (a) $Pr = 0.71$; (b) $Pr = 130$.

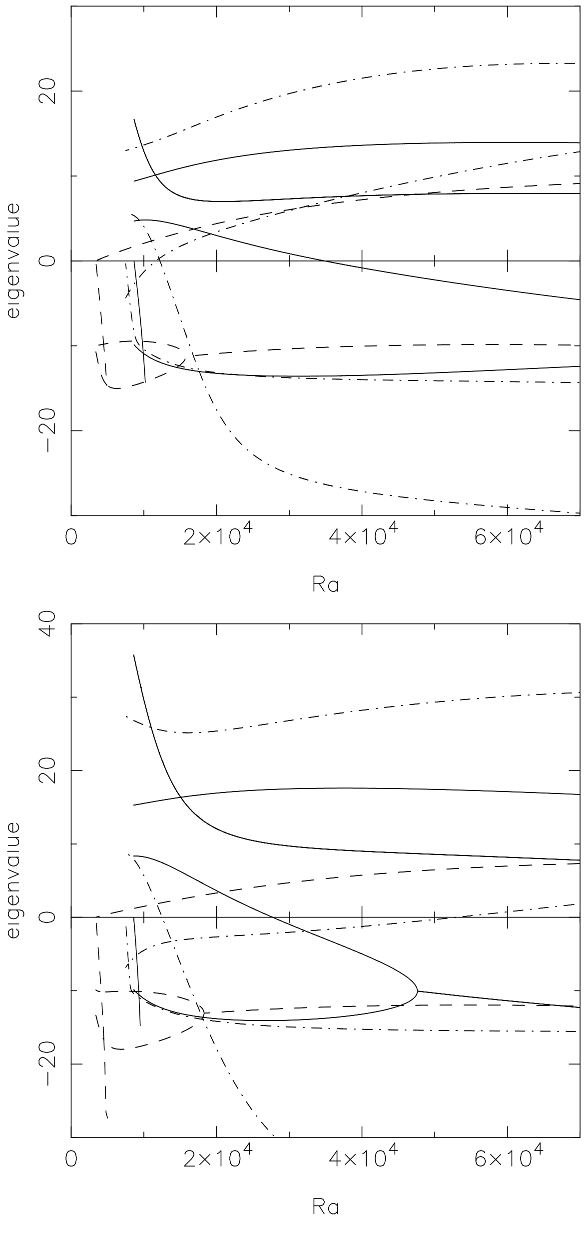

(a)

(b)

Figure 7: Variation of the real part of the principal eigenvalues for unstable structures $S2$ (dashed lines), $S4$ (dash-point lines) and $S6$ (solid lines) as a function of Ra: (a) $Pr = 0.71$; (b) $Pr = 130$.

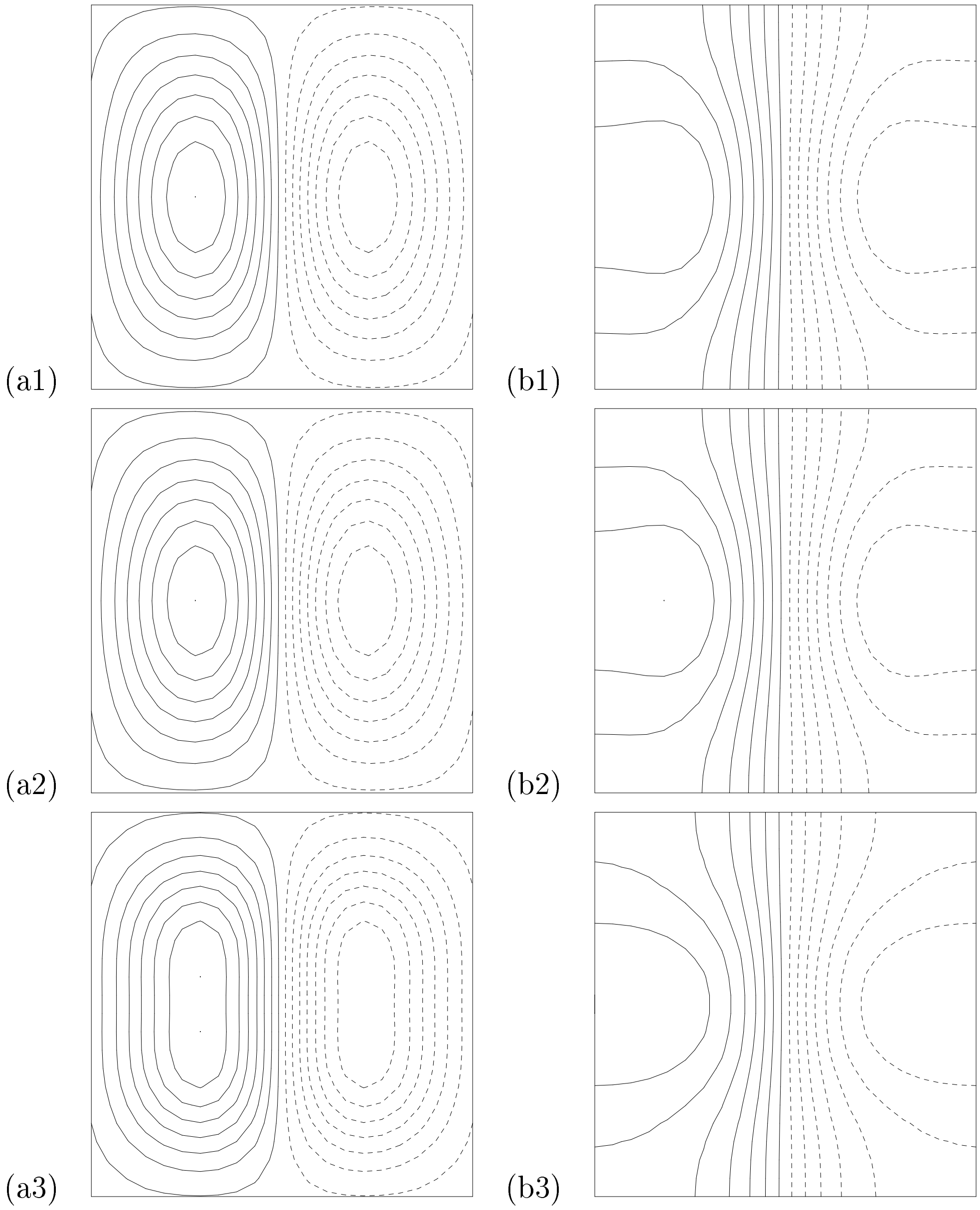

Figure 8: Vertical velocity contours (a1 to a3) and temperature contours (b1 to b3) in the horizontal midplane $z = 0$ for structure $S1$ at $Pr = 0.71$. Figures (a1-b1) and (a2-b2) show the contours predicted numerically by Pallar ès et al.[16] and by non–linear stability analysis at $Ra = 3500$. The contours predicted by linear stability analysis at $Ra_c = 3389$ are depicted in figures (a3-b3). Continuous and discontinuous lines refer to positive and negative values, respectively. The same convention has been used in the following Figures.

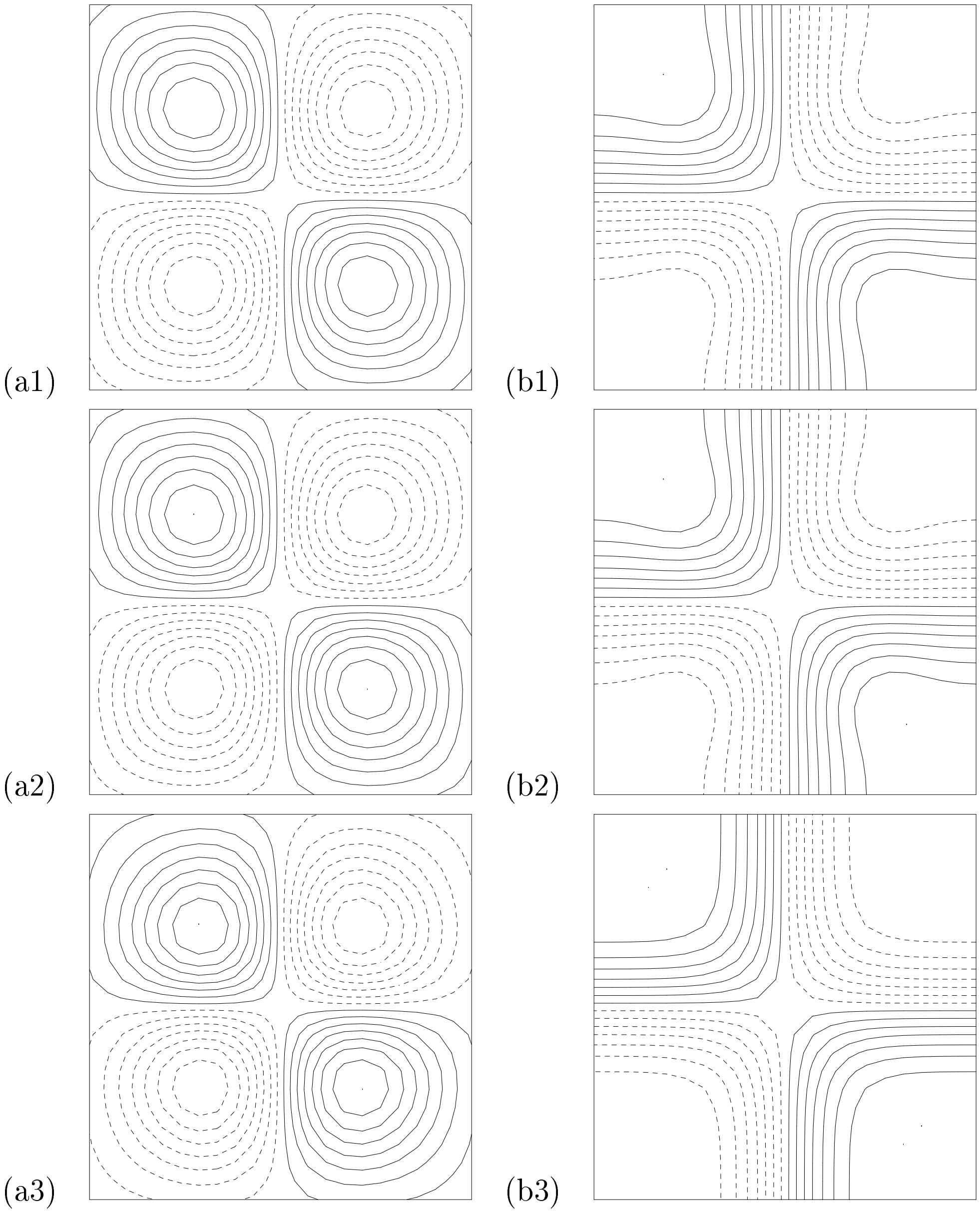

Figure 9: Vertical velocity contours (a1 to a3) and temperature contours (b1 to b3) in the horizontal midplane $z = 0$ for the structure $S5$ at $Pr = 0.71$. Figures (a1-b1) and (a2-b2) show the contours predicted numerically by Pallar ès et al.[16] and by non–linear stability analysis at $Ra = 6500$. The contours predicted by linear stability analysis at $Ra_c = 5902$ are depicted in figures (a3-b3).

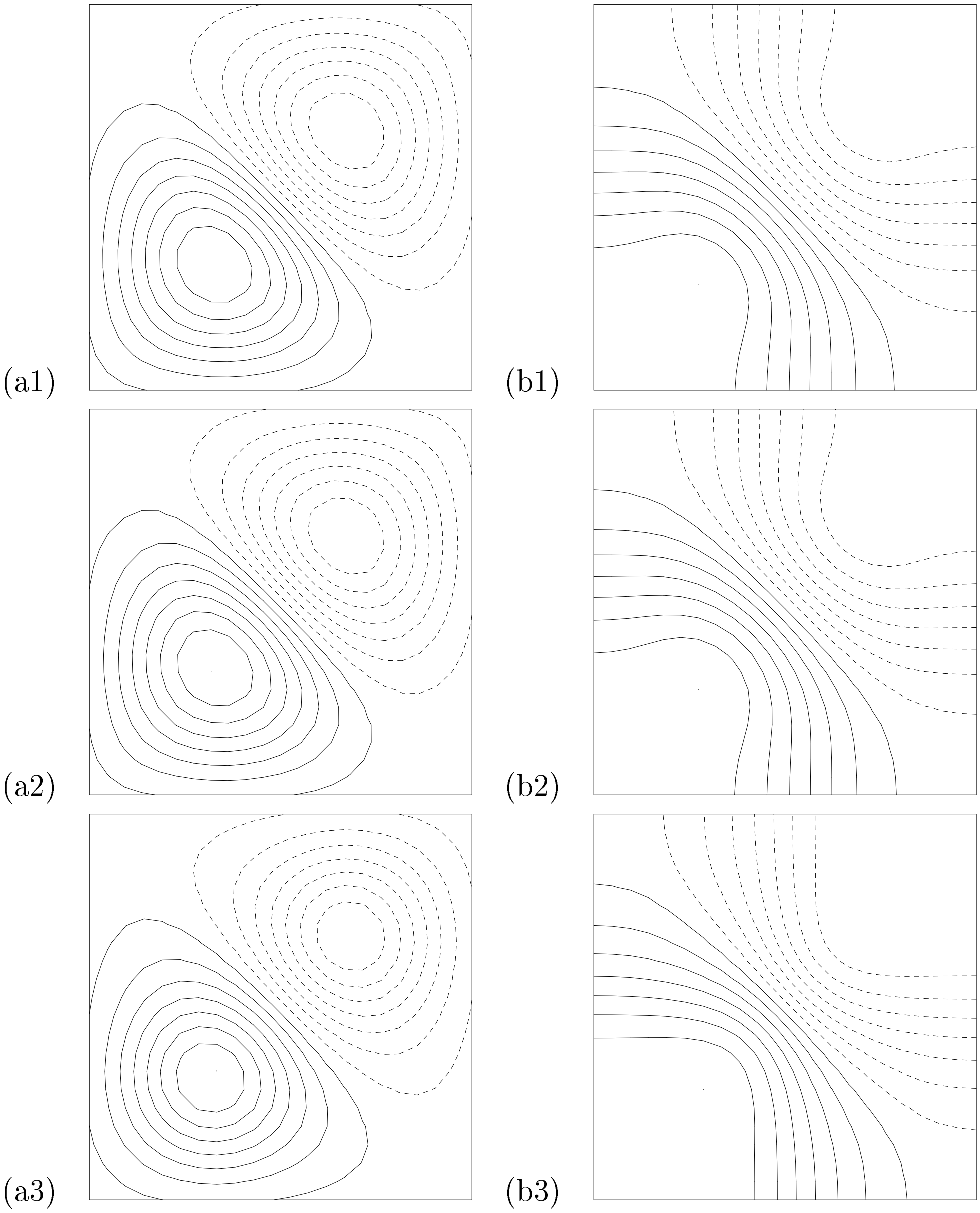

Figure 10: Vertical velocity contours (a1 to a3) and temperature contours (b1 to b3) in the horizontal midplane $z = 0$ for the structure $S2$ at $Pr = 0.71$. Figures (a1-b1) and (a2-b2) show the contours predicted numerically by Pallar ès et al.[16] and by non–linear stability analysis at $Ra = 3500$. The contours predicted by linear stability analysis at $Ra_c = 3389$ are depicted in figures (a3-b3).

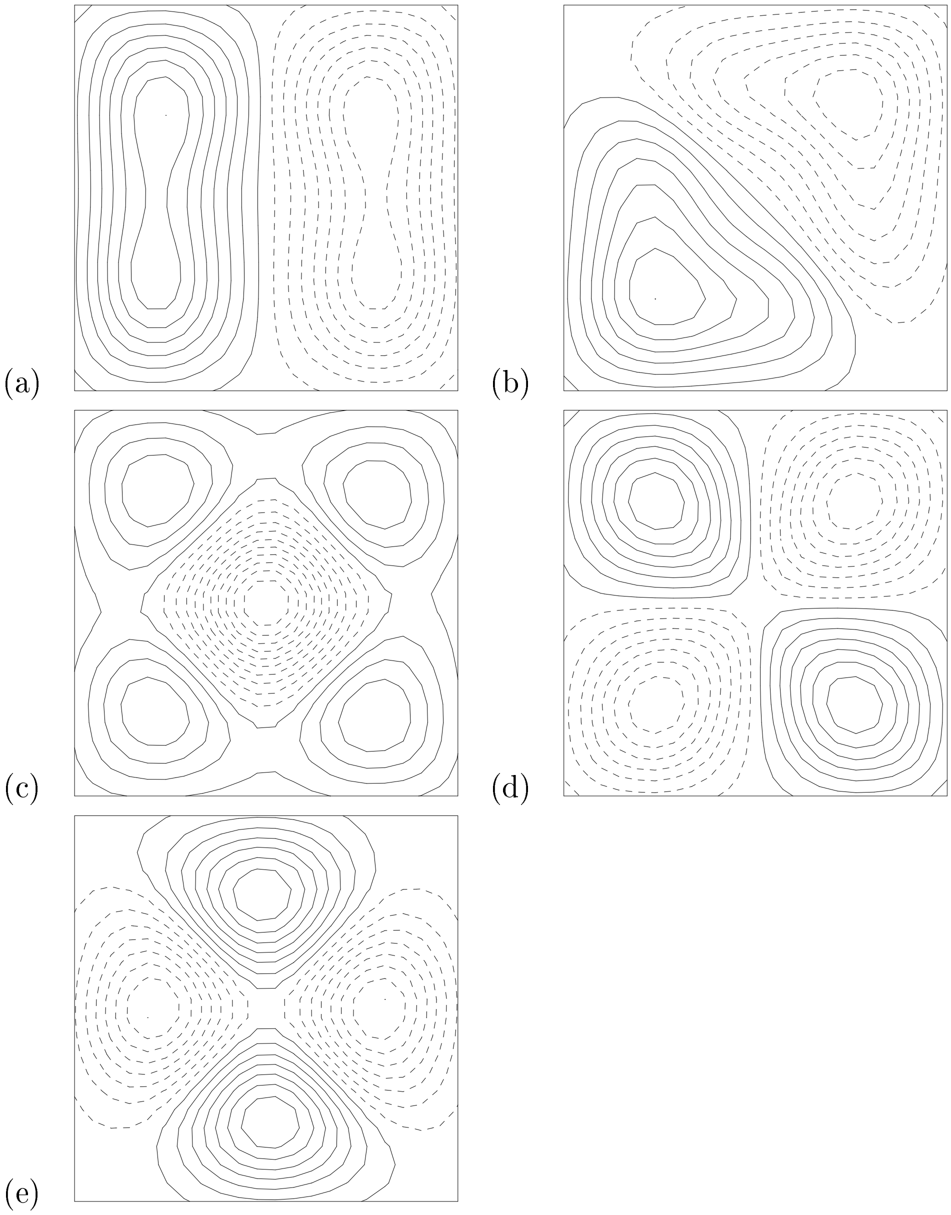

Figure 11: Vertical velocity contours in the horizontal midplane $z = 0$ predicted by non–linear stability analysis at $Ra = 70000$ and $Pr = 0.71$. (a) Structure $S1$; (b) structure $S2$; (c) structure $S4$; (d) structure $S5$; (e) structure $S6$.

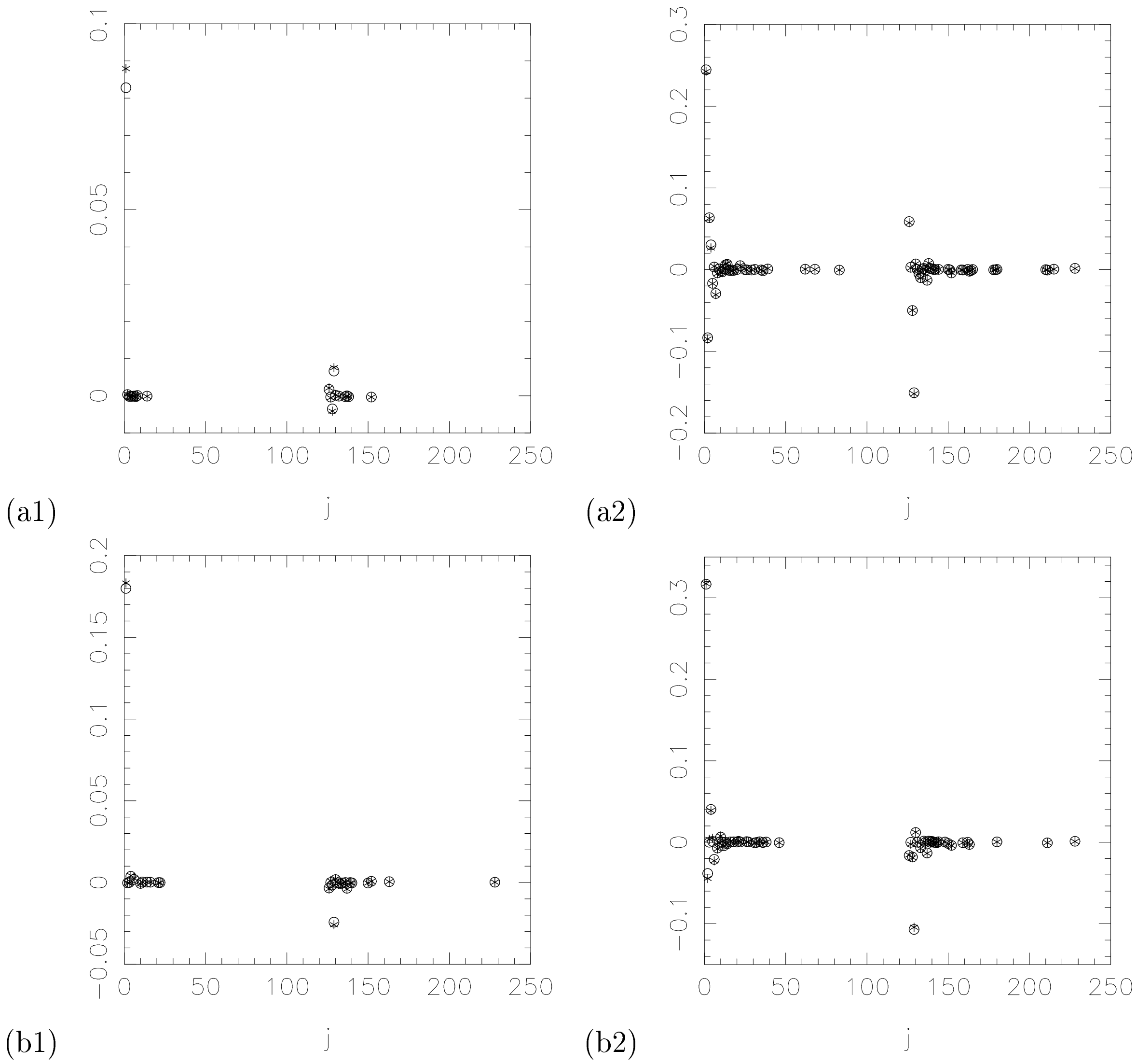

$*$ Numerical Results. $\circ$ Stability Analysis predictions.

Figure 12: Components of the projections of the stable flow structures predicted numerically onto the subspace generated by the trial functions at $Pr = 0.71$. (a1) Structure $S1$ at $Ra = 3500$; (a2) structure $S1$ at $Ra = 10^4$; (b1) structure $S5$ at $Ra = 6500$; (a2) structure $S5$ at $Ra = 10^4$. The index j indicates the number of the component. Only components larger than 10^{-3} times the greatest component have been considered.

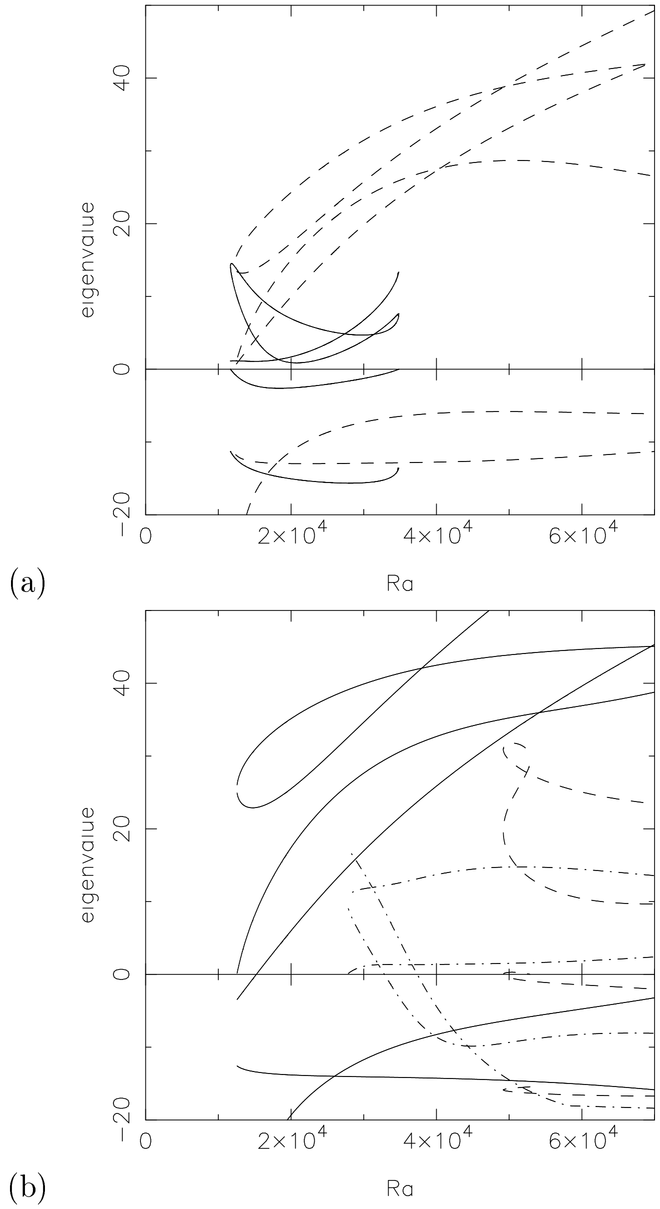

Figure 13: Variation of the real part of principal eigenvalues as a function of Ra for the unstable structures $S4a$ (solid lines), $S4b$ (dashed lines) and $S6a$ (dash-point lines). (a) $Pr = 0.71$; (b) $Pr = 130$. It should be noted that $S4a$ and $S6a$ coincide at $Pr = 0.71$.

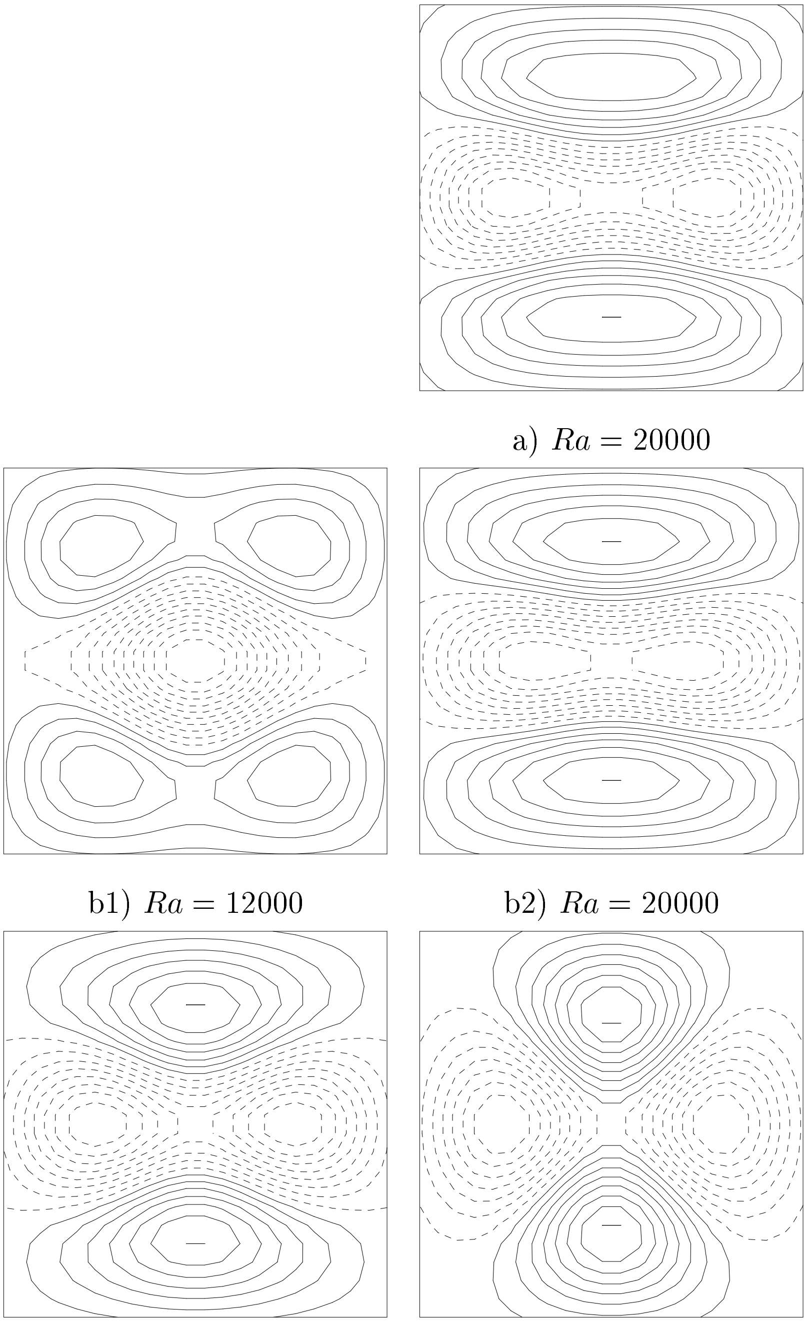

a) $Ra = 20000$

b1) $Ra = 12000$ b2) $Ra = 20000$

b3) $Ra = 30000$ b4) $Ra = 34809$

Figure 14: Vertical velocity contours in the horizontal midplane $z = 0$ for structure $S4a$ ($=S6a$) at $Pr = 0.71$. (a) Contours predicted numerically by Pallarès et al.[16]; (b1 to b4) contours predicted by non–linear stability analysis.